VOL. 27, NO. 9 AIAA JOURNAL SEPTEMBER 1989

Numerical Simulation of Vortical Flows Over a Strake-Delta Wing

Kozo Fujii* and Lewis B. Schiff†
NASA Ames Research Center, Moffett Field, California

Computations of vortical flows over a strake-delta wing are carried out using the three-dimensional, thin-layer Navier-Stokes equations at a low Mach number. A fine-mesh distribution with 850,000 grid points is used to capture the physical phenomenon, and computations are carried out for angles of attack from 6–40 deg. Over this range of angle of attack, the computed lift coefficients are in good agreement with the experimental data. A computed result at $\alpha = 12$ deg shows the interaction process of the vortex emanating from the leading edge of the strake with that from the leading edge of the wing. The computation at $\alpha = 30$ deg indicates that bubble-type vortex breakdown occurs near the trailing edge of the wing, whereas at $\alpha = 35$ deg, the spiral type of vortex breakdown occurs. An intensive study using sophisticated graphics programs reveals some features of the breakdown phenomenon. Comparison of the computed results with those of the experiment shows that qualitative features of the flow are well simulated when using a fine mesh. The result also indicates the importance of the grid resolution in simulating vortical flows. Still better resolution is necessary to obtain better quantitative results for this complicated flowfield.

Introduction

On slender wings at moderate to high angles of attack, the flow separates from the leading edge and forms a pair of spiral vortices above the upper surface of the wing. The low pressure induced on the upper surface by these separation vortices is the key factor in the nonlinear lift increase of fighter-type wings. At large angles of attack, breakdown of the leeward-side vortices occurs near the trailing edge. The vortex breakdown phenomenon causes both a loss in lift and an increased nose-up pitching moment. Although such vortical flows induced by the leading-edge separation are important research subjects, the basic mechanism is still not fully understood; current computational research is leading to an improved understanding of these flows and to the eventual control of vortex behavior.

The vortical flow associated with leading-edge separation is believed to be essentially convection-dominated flow (in other words, rotational inviscid flow), and thus methods that describe flow separation and inviscid rotational flow are feasible for this purpose. Recently, many simulations of such flowfields using three-dimensional Navier-Stokes equations have been reported.[1-4] The computed results indicate that these methods are capable of predicting a variety of vortical flowfields.

The Euler equations, which cannot describe flow separation mathematically, appear to give reasonable results because flow separates at the leading edge owing to the numerical dissipation. There has been a discussion about the causes of separation in the Euler solutions.[5-7] In Refs. 8 and 9, it is claimed that these solutions are essentially independent of the choice of dissipation, at least for sharp leading-edge geometries. One recognized defect of the Euler-solution approach is that it cannot capture the secondary separation vortex, which occurs near the leading edge. On the other hand, the Navier-Stokes equations are capable of describing all the separation vortices. In most computations, the thin-layer Navier-Stokes equations have been used, and recent computations by Thomas et al.[4] showed that vortex breakdown is simulated by the thin-layer Navier-Stokes equations.

In the present paper, three-dimensional, thin-layer Navier-Stokes computations for the vortical flowfields over a double-delta wing with sweep angles of 80 and 60 deg are presented. As shown schematically in Fig. 1, the flow surrounding a double-delta wing is more complicated than that surrounding a delta wing, since separation vortices emanate from both the strake leading edge and the wing leading edge. At moderate angles of attack, these two vortices interact with each other in the main wing region. The inboard vortex, originating from the strake leading edge, is relatively weak in the wing region; it is thus readily moved outboard by the induced velocity of the wing vortex, and the two vortices merge. When the angle of attack is increased, vortex breakdown occurs near the wing trailing edge. With further increase in angles of attack, the vortex breakdown moves forward and eventually occurs in the strake region. Two significant features of vortical flows are involved in this flowfield: vortex interaction and vortex breakdown.

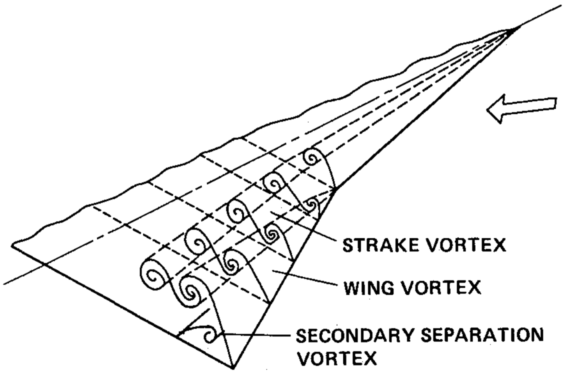

Fig. 1 Vortex system on strake-delta wing.

Presented as Paper 87-1229 at the AIAA 19th Fluid Dynamics, Plasma Dynamics, and Lasers Conference, Honolulu, HI, June 8–10, 1987; received June 18, 1987; revision received Aug. 15, 1988.

*National Research Council Postdoctoral Fellow; currently, Associate Professor, The Institute of Space and Astronautical Science, Sagamihara, Kanagawa, Japan. Member AIAA.

†Research Scientist, Fluid Dynamics Division. Associate Fellow AIAA.

To obtain numerical solutions for leading-edge vortical flowfields, both a powerful computer and an efficient computational method are needed. Two supercomputers, the Cray 2 at the Ames Research Center and the Amdahl 1200 at the Amdahl Corporation, have been used. The code based on the LU-ADI (lower-upper alternating direction implicit) algorithm (developed by one of the authors) is appropriate for this purpose; its reliability and efficiency have been demonstrated in extensive applications to many other flowfields.[10,11]

Governing Equations and Numerical Algorithm

Compressible Navier-Stokes Equations

The partial differential equations governing the unsteady three-dimensional flow of an ideal gas can be written in conservation-law form in a generalized coordinate system as

$$\partial_\tau \hat{Q} + \partial_\xi \hat{E} + \partial_\eta \hat{F} + \partial_\zeta \hat{G} = Re^{-1} \partial_\zeta \hat{S} \tag{1}$$

where $\hat{Q}, \hat{E}, \hat{F}, \hat{G}$, are

$$\hat{Q} = J^{-1} \begin{bmatrix} \rho \\ \rho u \\ \rho v \\ \rho w \\ e \end{bmatrix}, \qquad \hat{E} = J^{-1} \begin{bmatrix} \rho U \\ \rho u U + \xi_x p \\ \rho v U + \xi_y p \\ \rho w U + \xi_z p \\ U(e+p) - \xi_t p \end{bmatrix}$$

$$\hat{F} = J^{-1} \begin{bmatrix} \rho V \\ \rho u V + \eta_x p \\ \rho v V + \eta_y p \\ \rho w V + \eta_z p \\ V(e+p) - \eta_t p \end{bmatrix}, \qquad \hat{G} = J^{-1} \begin{bmatrix} \rho W \\ \rho u W + \zeta_x p \\ \rho v W + \zeta_y p \\ \rho w W + \zeta_z p \\ W(e+p) - \zeta_t p \end{bmatrix}$$

$$\hat{S} = J^{-1} \begin{bmatrix} 0 \\ \mu m_1 u_\zeta + (\mu/3) m_2 \zeta_x \\ \mu m_1 v_\zeta + (\mu/3) m_2 \zeta_y \\ \mu m_1 w_\zeta + (\mu/3) m_2 \zeta_z \\ \mu m_1 m_3 + (\mu/3) m_2 (\zeta_x u + \zeta_y v + \zeta_z w) \end{bmatrix}$$

Here $m_1 = \zeta_x^2 + \zeta_y^2 + \zeta_z^2$; $m_2 = \zeta_x u_\zeta + \zeta_y v_\zeta + \zeta_z w_\zeta$; $m_3 = (u^2 + v^2 + w^2)_\zeta / 2 + \kappa Pr^{-1} (\gamma - 1)^{-1} (a^2)_\zeta$; and U, V, and W are unscaled contravariant velocities.

In Eq. (1), the thin-layer approximation has been introduced. The use of thin-layer Navier-Stokes equations for high-Reynolds-number flow simulations is justified because the viscous effects are confined to a thin layer near the wall boundary and are dominated by the viscous terms associated with the strain rates normal to the wall, and because the flow away from the body is essentially rotational and inviscid. Although viscosity effects exist in the vortex sheets that emanate from separation lines at the wing leading edge and roll up to form the leeward vortices, these effects are assumed to be small in comparison to the convective effects of the external (inviscid) pressure field. Furthermore, the viscous stress terms cannot be accurately evaluated in these regions, even using the full Navier-Stokes equations, since the computational grid is not sufficiently fine.

The pressure, density, and velocity components are related to the energy for an ideal gas by

$$p = (\gamma - 1)[e - \rho(u^2 + v^2 + w^2)/2] \tag{2}$$

In the following computations, flow is assumed to be laminar and no turbulence model is used. The spatial metrics are evaluated using second-order central-difference formulas for interior points and three-point, one-sided formulas at the boundaries. Solutions of Eq. (1) are obtained by time integration.

LU-ADI Factorization Algorithm

The numerical algorithm used here is the new LU-ADI factorization method proposed by Fujii and Obayashi.[10,11] Implicit time-integration methods in so-called delta form are widely used for solving steady-state problems since the steady-state solutions are indifferent to the left-hand-side operators. The most commonly used method is the approximate-factorization technique originally proposed by Beam and Warming and used in Ref. 12. The present LU-ADI factorization method belongs to a category of the schemes that reduce the work of inverting the left-hand-side operators of the Beam-Warming method. Each ADI operator is decomposed into the product of lower and upper bidiagonal matrices by using a flux-vector splitting technique and a diagonally dominant factorization. It should be noted that central differencing is used in the right-hand side as in Ref. 12.

The Beam-Warming factorization applied to Eq. (1) is written as

$$\begin{aligned} &(I + h\delta_\xi \hat{A}^n - D_i|_\xi)(I + h\delta_\eta \hat{B}^n - D_i|_\eta) \\ &\quad \times (I + h\delta_\zeta \hat{C}^n - hRe^{-1}\bar{\delta}_\zeta J^{-1}\hat{M}^n J - D_i|_\zeta)\Delta\hat{Q}^n \\ &\quad = -h(\delta_\xi \hat{E}^n + \delta_\eta \hat{F}^n + \delta_\zeta \hat{G}^n - Re^{-1}\bar{\delta}_\zeta \hat{S}^n) \\ &\quad -(D_e|_\xi + D_e|_\eta + D_e|_\zeta)\hat{Q}^n \end{aligned} \tag{3}$$

where h is the time step and δ a central finite-difference operator. The D_i and D_e terms are implicit and explicit artificial dissipation terms that should be added to the left-hand side and the right-hand side, respectively, to maintain stability. The basic algorithm is first-order accurate in time and second-order accurate in space. For the convective terms in the right-hand side, fourth-order differencing is used except near the boundaries. Maintenance of the freestream is achieved by subtracting the freestream fluxes from the governing equations.

In the LU-ADI algorithm, each ADI operator is rewritten using the diagonal form[10,13] and the flux-vector splitting technique.[14] For example, in the ξ direction,

$$\begin{aligned} &I + h\delta_\xi \hat{A} \\ &\quad \doteq T_\xi (I + h\delta_\xi^b \hat{D}_A^+ + h\delta_\xi^f \hat{D}_A^-) T_\xi^{-1} \\ &\quad \doteq T_\xi (I - \alpha h \hat{D}_{Aj}^- + h\delta_\xi^b \hat{D}_A^+)(I + \alpha h |\hat{D}_{Aj}^-|)^{-1} \\ &\quad \times (I + \alpha h \hat{D}_{Aj}^+ + h\delta_\xi^f \hat{D}_A^-) T_\xi^{-1} \end{aligned} \tag{4}$$

where α is a coefficient appearing on the j index for the upwind differencing. In other words, $\alpha = 1.0$ when first-order differencing is used for the ξ derivative and 1.5 when second-order differencing is used. Currently, α is set to be 7/6, since three-point, first-order differencing is used for the ξ derivative in order to be consistent with the fourth-order differencing in the right-hand-side convective terms. The decomposition used in Eq. (4) can be called approximate LDU factorization or diagonally dominant factorization. This decomposition is more stable than simple LU factorization because the diagonal element always has $|\hat{D}_A|$.

In the solution process, an inversion in one direction consists of one scalar forward sweep and one scalar backward sweep. Thus, the LU-ADI algorithm requires little additional memory and is easily vectorized. It may be noteworthy that an operator in each direction can be considered to be a single iteration of a symmetric Gauss-Seidel relaxation in one dimension.

The $\hat{D}_A^\pm$ terms are modified to include an implicit artificial dissipation term. Another modification is necessary in the ζ direction to evaluate implicit viscous terms. Additional details of the derivation of the LU-ADI algorithm are given in Ref. 10.

The artificial dissipation model developed in Ref. 11 is used in this study. This dissipation model is of a nonlinear, second- and fourth-order mixed type. To suppress the second-order smoothing terms in the global flowfield, a limiter function is introduced based on the simplified idea of a total variation diminishing scheme. In the left-hand side, only the fourth-order smoothing is included. Details of this artificial dissipation are provided in Ref. 11.

Results

Grid Topology and Boundary Conditions

The body geometry in the present study is a double-delta wing shown in Fig. 2 in terms of the surface-grid distribution. The leading-edge sweep angle is 80 deg at the strake and 60 deg at the wing. The thickness is 0.6% of the chord, and the leading edge is rounded. This body geometry is the same as that used in the experiment by Brennenstuhl and Hummel[15] and is very similar to that used in a water-tank experiment by Thompson,[16] except for a slightly different wing thickness.

A perspective view of the discretized region is shown in Fig. 3. The grid topology is cylindrical, that is, it is of the H-type in the chordwise direction and O-type in the spanwise direction. A typical cross-sectional view (at $x/c \approx 0.95$) is shown in Fig. 4. The computational grid is generated by the two-dimensional hyperbolic grid-generation method for each chordwise station.[17] To accurately describe the body geometry, the surface grid is carefully distributed, especially in the apex, leading-edge, and trailing-edge regions.

The grid extends approximately 2 root chords upstream, 3 chords downstream, and 2.5 chords above, below, and outward of the wing. The locations of the outer boundaries are not far from the body but are probably adequate. There may be an influence of the outer boundary on the solutions, especially at large angles of attack, but the global flow structure should not change. The influence of the outer boundary on the solutions needs further investigation. Freestream values are specified along the upstream and circumferential boundaries; the pressure is fixed, and the other physical variables are extrapolated at the outflow boundary.

Bilateral symmetry is imposed to reduce the computational domain. It is recognized that when very slender delta wings are placed at high incidence (wing sweep angles greater than 75 deg), asymmetric vortex flows can occur even at zero sideslip. Simulation of such asymmetric flows, and of flows over wings at nonzero sideslip, will require including the entire body in the computation.

The grid consists of 119 points in the chordwise (ξ) direction (14 points upstream of the body, 76 points over the body, and 29 points in the wake), 101 points in the circumferential (η) direction, and 71 points in the radial (ζ) direction.

In the computations reported in this paper, a Mach number of 0.3 is used so that comparison can be made with the low-speed experiment.[15] There may be a slight compressibility effect in the computations reported herein, but this should not change the basic flow structure. The Reynolds number based on the root chord length c is 1.3×10^6, corresponding to that of the experiment. Preliminary computations showed evidence of flow unsteadiness for high-angle-attack cases. In order to resolve the unsteadiness, a constant time-step ($\Delta t = 0.01$) was used rather than the spatially varying time steps.

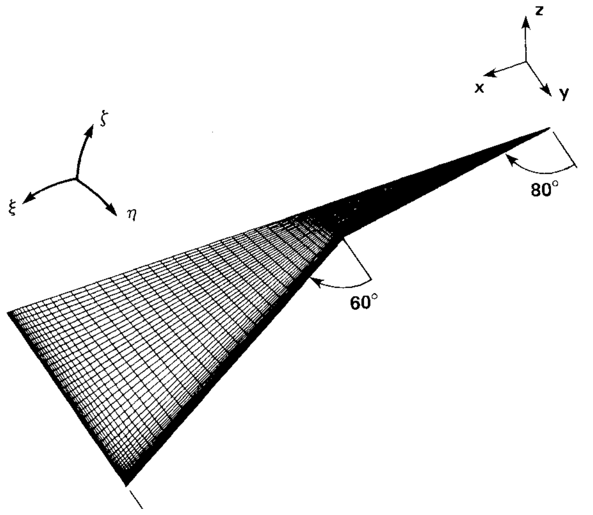

Fig. 2 Body geometry and surface grid distribution for the strake-delta wing.

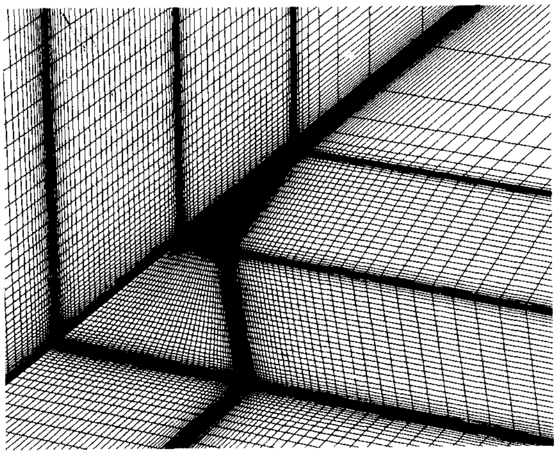

Fig. 3 Close-up view of the discretized region: $x/c \approx 0.95$.

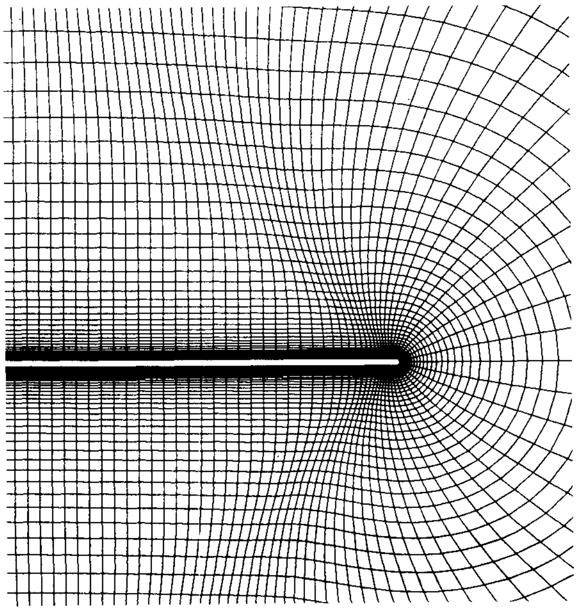

Fig. 4 Typical cross-sectional view of the grid distributions.

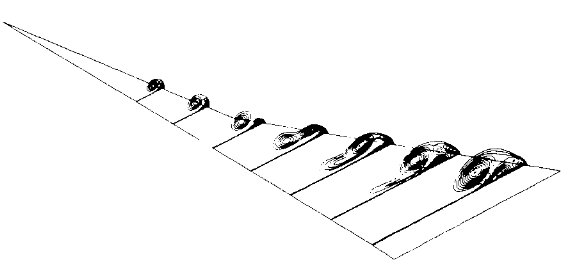

Fig. 5 Perspective view of the spanwise total-pressure contour plots: $M_\infty = 0.3$, $Re = 1.3 \times 10^6$, $\alpha = 12.0$ deg.

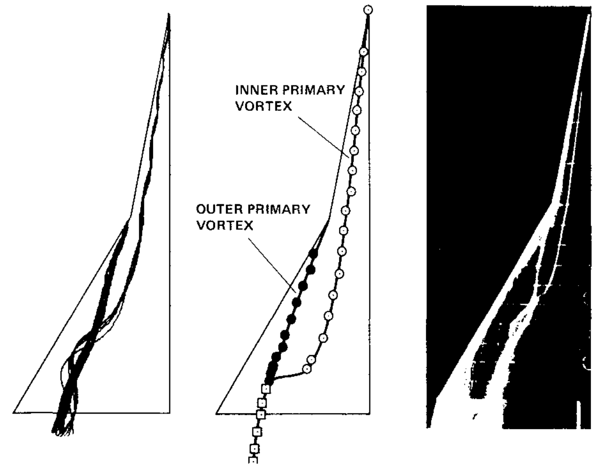

(a) COMPUTATION (Re = 1.3 X 10^6) (b) EXPERIMENT[15] (Re = 1.3 X 10^6) (c) EXPERIMENT[16] (Re = 1.0 X 10^5)

Fig. 6 Computed off-surface particle path pattern: $M_\infty = 0.3$, $Re = 1.3 \times 10^6$, $\alpha = 12.0$ deg.

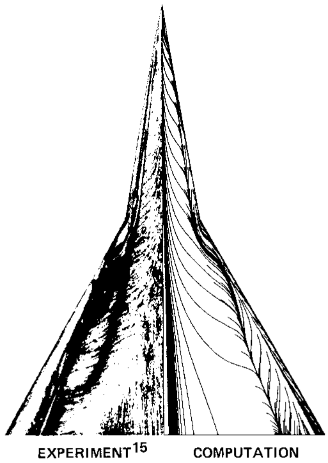

Fig. 7 Computed near-surface flow pattern vs experimental surface oil-flow pattern: $M_\infty = 0.3$ (incompressible in the experiment), $Re = 1.3 \times 10^6$, $\alpha = 12.0$ deg.

Computed Result: $\alpha = 12$ Deg

The perspective view of the total-pressure contour plots at several chordwise stations at $\alpha = 12$ deg is shown in Fig. 5. Total-pressure contour plots are frequently used in both experiments and computations because they are good indicators of the presence of vortices. At this angle of attack, two vortices are observed: one from the strake and the other from the wing leading edge. The strength of the wing vortex increases with increasing distance downstream of the strake-wing junction. As the strength of the wing vortex increases, the weaker strake vortex is drawn downward and outward because of the velocity field induced by the wing vortex. At the downstream station, the strake vortex is observed to have merged with the wing vortex. The total-pressure loss owing to the secondary separation vortex is also clearly seen in the two downstream stations shown in Fig. 5.

The computed off-surface particle traces for this case are shown in Fig. 6a, together with the locus of vortices measured experimentally by Brennenstuhl and Hummel[15] at the same Reynolds number (Fig. 6b). Also shown in Fig. 6c is the water-tank flow visualization obtained by Thompson[16] at a lower Reynolds number ($Re = 1.0 \times 10^5$) on a similar model. The merging of the vortices is well simulated qualitatively; however, the computed station at which the merging occurs is upstream of that observed in Ref. 12 and closer to that visualized at the lower Reynolds number.

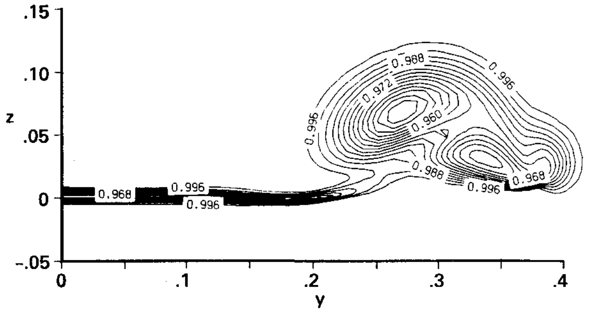

(a) COMPUTATION

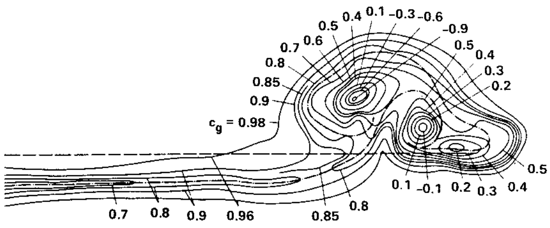

(b) EXPERIMENT[15]

Fig. 8 Total-pressure contour plots in the crossflow plane 10% chord behind the trailing edge: $M_\infty = 0.3$, $Re = 1.3 \times 10^6$, $\alpha = 12.0$ deg.

The most likely source of the discrepancy between the computed and experimental results is the fact that the flow was assumed to be laminar in the computation, whereas the flow was probably transitional in the experiment. Note that the computed wing vortex is located farther inboard than the experimental one. Although the primary separation lines are essentially fixed at the wing leading edge for a thin delta wing, transition to turbulent flow causes the secondary separation on the wing to occur farther outboard; as a result, the primary vortices are located outboard and downward above the wing (cf. Ref. 18). Similarly, as discussed in detail by Thompson,[16] an increase of laminar Reynolds number causes the position of the wing vortex to move outboard and downward and thus causes the merging point to move downstream. Since the computed wing vortex is located inboard of that observed in the experiment in Ref. 15, it is consistent with the experimental trend that computed vortices merge farther upstream in the present result. An investigation of the effect of turbulence with fine-grid computations using a suitable turbulence model (cf. Ref. 19) is a subject for further work. It should be noted that the position of the vortex axes in Ref. 15 was determined by moving the probe into the total-pressure minimum. Examination of computed results in Figs. 5 and 6a shows that the use of the total-pressure criterion indicates vortex merging to be downstream of that shown by particle traces.

The computed surface-flow pattern is compared with the experimental oil-flow visualization of Ref. 15 in Fig. 7. The flow pattern induced by the primary separation vortex and the secondary separation vortex is well simulated. The discrepancy of the spanwise location of the lines of the secondary separation vortex is consistent with the assumption of laminar flow in the computation. Another useful comparison is the wake pattern. Total-pressure contours in a crossflow plane normal to the wing surface, located downstream of the wing trailing edge ($x/c = 1.10$), are shown in Fig. 8a. The corresponding experimental contours, obtained at the same downstream station in a plane normal to the freestream, are shown in Fig. 8b. It is clear that the main flow features are well simulated, even though quantitative comparison is difficult because the planes are not identically inclined and the contour levels are different.

The surface-pressure plots (not shown here) indicated that the computed strake vortex is weaker than that of the experiment. Downstream of the strake-wing junction, the strake vortex is no longer fed by vorticity shed from the leading edge; it remains constant in strength or may weaken owing to viscous effects. The current grid resolution and spatial accuracy of the computational scheme are not enough to capture this process accurately. As a result, the vortex tends to lose its strength rapidly because of the numerical dissipation. A recent paper by Rai[20] goes into more detail about the difficulty of simulating vortical flowfields.

Computed Result: $\alpha = 30$ Deg

The perspective view of the total-pressure contour plots at $\alpha = 30$ deg is shown in Fig. 9. At this angle of attack, the merging of the strake and wing vortices occurs near the strake-wing junction. An abrupt change of the flow is observed at about $x/c = 0.85$, where the vortex core suddenly becomes large. This indicates that the primary vortex has undergone breakdown. Computed off-surface particle-path traces shown in Fig. 10 clearly confirm the breakdown of the primary vortex. The off-surface flow visualization by Thompson[16] for the same planform geometry is also presented in Fig. 10. It should be noted that the experimental Reynolds number is lower and that weak asymmetry of the flow is observed in the experiment. The vortex from the strake region is well ordered and very tightly coiled to about 80 or 85% of chord, where an abrupt change of the flow is observed. In addition to the particles released from the leading edges of the strake and wing, particles are released from the trailing-edge region. Some of these particles move upstream to about 85% chord and then move back downstream to the trailing-edge region. It should be noted that these reverse-flow particles continue to swirl along with the general motion of the vortex, although the swirling is weak. It is also noticed that the strake vortex moves outward just after the kink point, because of the interaction with the wing vortex.

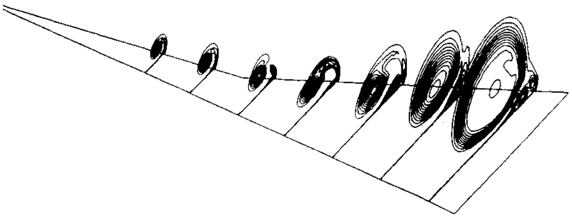

Fig. 9 **Perspective view of the spanwise total-pressure contour plots: $M_\infty = 0.3$, $Re = 1.3 \times 10^6$, $\alpha = 30.0$ deg.**

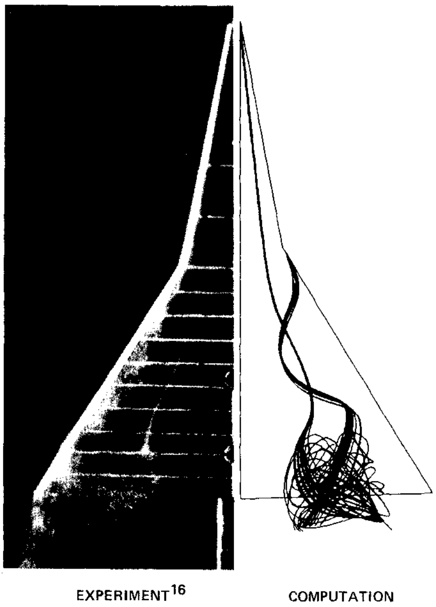

Fig. 10 **Computed off-surface particle path pattern: $M_\infty = 0.3$, $Re = 1.3 \times 10^6$, $\alpha = 30.0$ deg.**

Figure 11 shows the computed surface-flow patterns for this case, compared with the experimental oil-flow visualization.[15] In contrast to the lower-angle-of-attack case, the flow induced by the main vortex has an almost zero streamwise component upstream of $x/c = 0.8$ and collides with the flow induced by

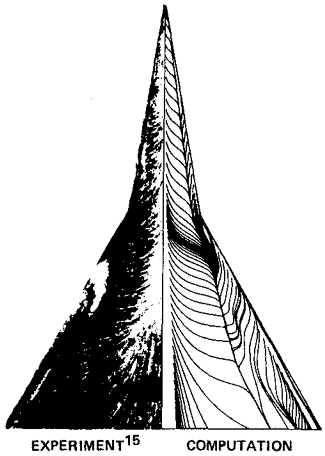

Fig. 11 **Computed near-surface flow pattern vs experimental surface oil-flow pattern: $M_\infty = 0.3$ (incompressible in the experiment), $Re = 1.3 \times 10^6$, $\alpha = 30.0$ deg.**

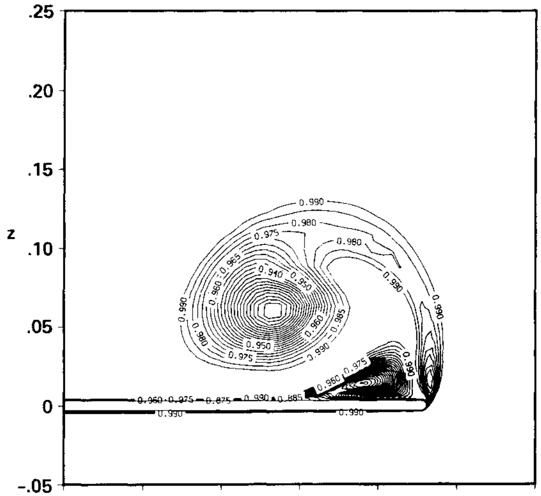

(a) TOTAL PRESSURE CONTOURS

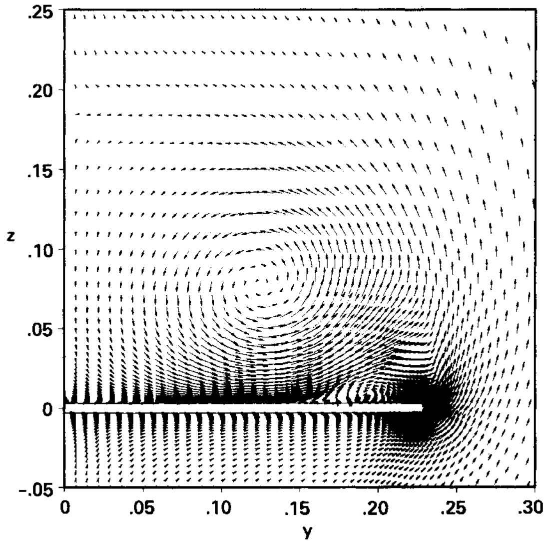

(b) VELOCITY VECTORS

Fig. 12 **Computed results in the crossflow plane at 75% chordwise station: $M_\infty = 0.3$, $Re = 1.3 \times 10^6$, $\alpha = 30.0$ deg.**

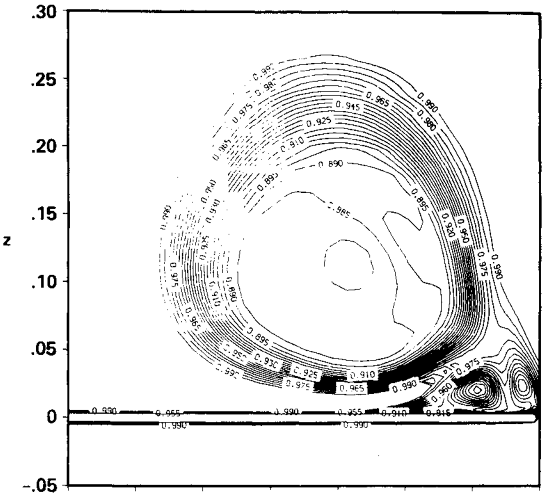

(a) TOTAL PRESSURE CONTOURS

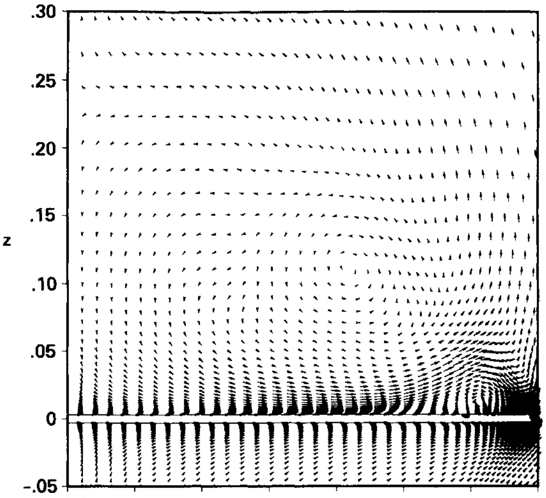

(b) VELOCITY VECTORS

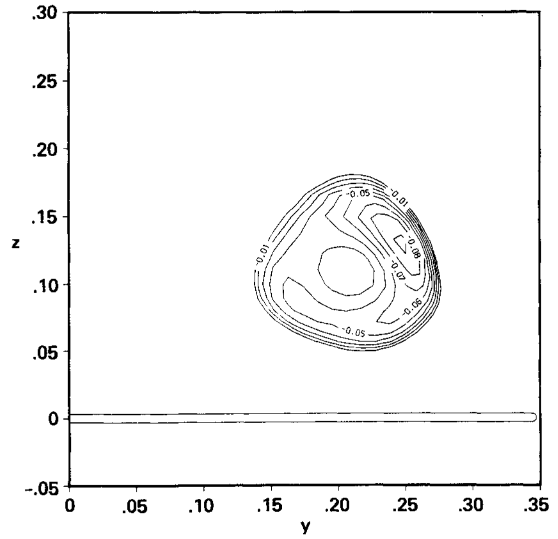

(c) NEGATIVE u-VELOCITY CONTOURS

Fig. 13 Computed results in the crossflow plane at 95% chordwise station: $M_\infty = 0.3$, $Re = 1.3 \times 10^6$, $\alpha = 30.0$ deg.

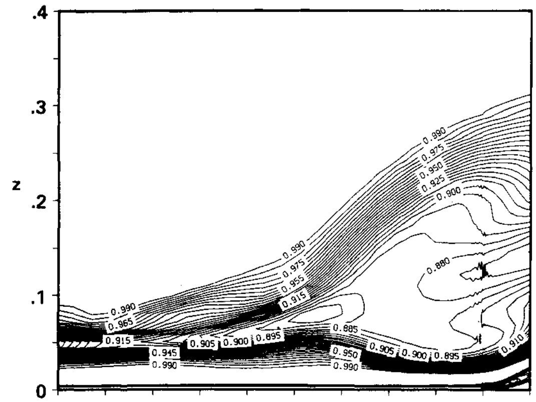

(a) TOTAL PRESSURE CONTOURS

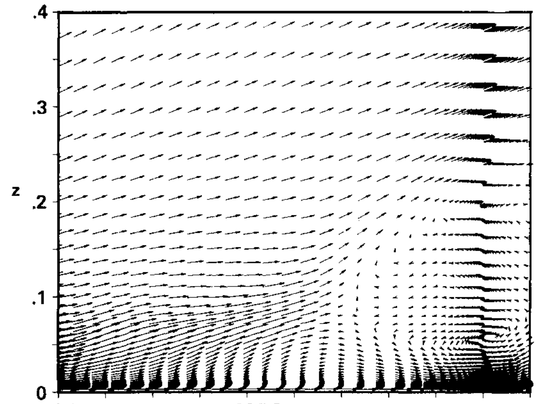

(b) VELOCITY VECTORS

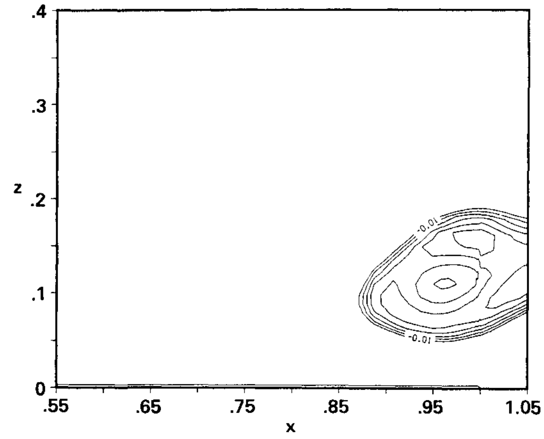

(c) NEGATIVE u-VELOCITY CONTOURS

Fig. 14 Computed results in the longitudinal cross section through breakdown: $M_\infty = 0.3$, $Re = 1.3 \times 10^6$, $\alpha = 30.0$ deg.

the secondary separation vortex. Downstream of $x/c = 0.8$, there is a large change in the spanwise slope of the surface flow. It is apparent that the strength of the swirling flow becomes weaker downstream of this station.

Spanwise total-pressure contour plots and the velocity-vector plots at $x/c = 0.75$ are shown in Figs. 12a and 12b, respectively. This chordwise station is located upstream of the breakdown. Both figures clearly show the strong primary vortex and the secondary separation vortex. Analogous plots at the streamwise station located at $x/c = 0.95$, downstream of the vortex breakdown, are shown in Figs. 13a and 13b. Contour plots representing the region of negative (upstream) axial u-velocity components are shown in Fig. 13c. In contrast to Figs. 12a and 12b, the size of the vortex core is gradually increased, and the core has a large region of almost constant total pressure. The secondary-separation vortex seems to be unaffected by the vortex breakdown. Figure 13c indicates that streamwise reverse flow occurs in the center of the vortex. Figures 14a-14c show the total-pressure contour plots, the velocity-vector plots, and the negative u-velocity contour plots in the constant-η plane (longitudinal cross section) that passes through the center of the vortex. Two symmetric recirculating regions are located just downstream of the stagnation point. Thus, for this case, the breakdown appears similar to a bubble-type breakdown.

To check the effect of the smoothing terms, the coefficients of the smoothing terms are artificially increased by a factor of 3. The result, which showed the existence of the vortex breakdown, is close to the result shown in Fig. 9, except that the secondary-separation vortex is smaller. This indicates that the smoothing terms are not the key flowfield-determining factors. The viscous shear layers over the surface appear to be the most important factor in deciding the vortical flow.

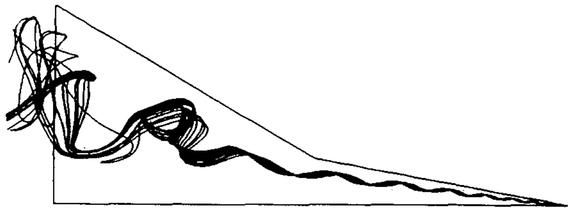

Fig. 15 Computed off-surface partical path pattern: $M_\infty = 0.3$, $Re = 1.3 \times 10^6$, $\alpha = 35.0$ deg.

It is well recognized that the computational grid spacing must be adequate to resolve the significant features of the flowfield. In many flowfields, the important physical phenomena occur only near the body surface. Current computer capability permits adequate grid resolution, even for complicated body geometries, on such problems. On the other hand, for separated vortical flows, significant flow features that determine the flow characteristics occur in the region away from the body. Current grid resolutions may not be adequate, even for simple body geometries. For the $\alpha = 30$ deg case, the effect of grid resolution on the ability of the thin-layer Navier-Stokes code to simulate vortex breakdown was investigated. In addition to the fine-grid solution discussed above, computations were carried out using a coarse-grid ($41 \times 33 \times 27$) and a medium-grid ($63 \times 61 \times 41$) distribution. Neither the medium nor the coarse grid solutions showed evidence of axially reversed flow, and neither showed evidence of increased size of the vortex core. Thus, it appears that at a minimum, a grid resolution like the fine grid used in this study is necessary to capture the vortex breakdown. Details of the grid-refinement study are reported in Ref. 21.

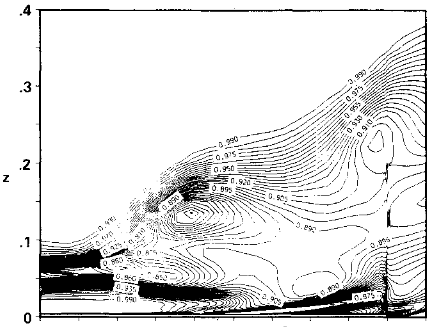

(a) TOTAL PRESSURE CONTOURS

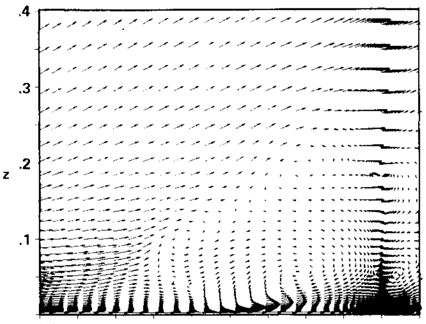

(b) VELOCITY VECTORS

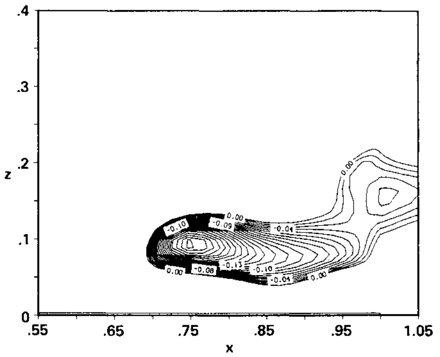

(c) NEGATIVE u-VELOCITY CONTOURS

Fig. 16 Computed results in the longitudinal cross section through breakdown: $M_\infty = 0.3$, $Re = 1.3 \times 10^6$, $\alpha = 35.0$ deg.

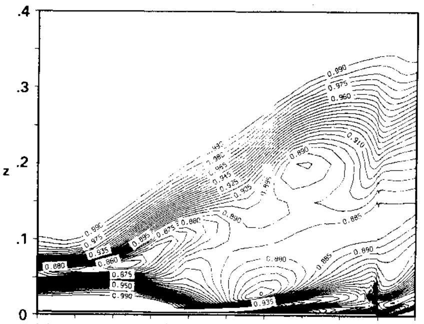

(a) TOTAL PRESSURE CONTOURS

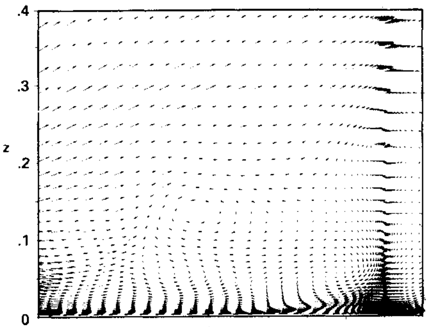

(b) VELOCITY VECTORS

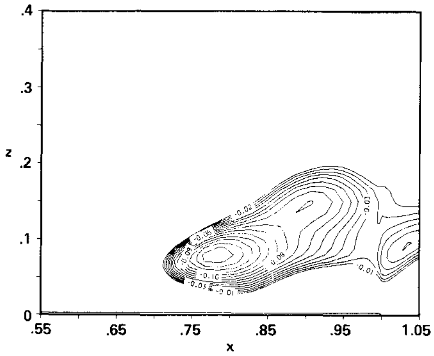

(c) NEGATIVE u-VELOCITY CONTOURS

Fig. 17 Computed results in the longitudinal cross section (240 iterations later): $M_\infty = 0.3$, $Re = 1.3 \times 10^6$, $\alpha = 35.0$ deg.

Computed Results: $\alpha = 35$ Deg

The top view of the off-surface particle-path traces at $\alpha = 35$ deg is shown in Fig. 15. The breakdown now takes place at about $x/c = 0.6$. The core flow from the strake leading edge has an abrupt kink there and forms a large spiral. A large vertical spiral inside the breakdown region is also observed. Additional details of the flow structure of the breakdown can be seen in the total-pressure contour plots, velocity-vector plots, and negative u-velocity contour plots in the longitudinal cross section shown in Figs. 16a-16c, respectively. The reverse-flow region does not create a bubble shape but creates an alternative recirculation pattern similar to that obtained by cutting a helix with a plane. A small recirculating region is observed below and downstream of the abrupt kink of the core flow, and a larger recirculating region is observed above and farther downstream, and so on. It is obvious that the flowfield at $\alpha = 35$ deg shows a different type of breakdown from that at $\alpha = 30$ deg. In contrast to the solution at $\alpha = 30$ deg, the flow unsteadiness is more pronounced. Figures 17a-17c show the result at 240 iterations after the result shown in Fig. 16. Small recirculation regions have changed their locations. This implies that these vortices are moving in time, which is typical of a spiral-type breakdown. Even though there is no clear evidence, the result seems to indicate the existence of the spiral-type breakdown (see Figs. 12a, 12b, 14a, and 14b in Ref. 22 for comparison). It should be noted that the secondary-separation vortex is distorted by the existence of the breakdown in this case.

Computed Vortex Breakdown Types

When comparing Figs. 14a, 16a, and 17a, one remarkable difference between the 30 deg result and 35 deg result is observed. At $\alpha = 30$ deg (Fig. 14a), the recirculating region sitting in the bubble breakdown is away from the surface. On the other hand, at $\alpha = 35$ deg (Figs. 16a and 17a), the lower recirculating spiral is located near the wing surface and the interaction of the spiral vortex and the wing surface occurs. As a result, contours become dense near the wing surface as shown in Figs. 16a and 17a, and a jetlike velocity profile is observed in Figs. 16b and 17b. This interaction may have caused the spiral-type breakdown. Further investigation is needed to draw conclusions.

The structure of the vortex breakdown is not fully understood. In an experiment on a delta wing, for instance, it was reported that both spiral and bubble types of breakdowns were seen to transform from one to the other at random.[22] The effect of turbulence is one factor that is always an issue. The computation assumes laminar flow, and the grid resolution is not fine enough to capture small eddies associated with the turbulent flow. However, the global vortical flow structures remain similar both for laminar and turbulent flows. Thus, the computed solutions may be useful in understanding the flow structure, although strict quantitative comparison with the experiment is difficult.

Lift Characteristics and Flow Unsteadiness

Figure 18 shows the lift coefficient C_L as a function of angle of attack α for the present Navier-Stokes solutions and for experimental data.[15] Also shown in Fig. 18 are the results of Euler computations. These Euler solutions are discussed later. Navier-Stokes results show good agreement up to $\alpha \approx 27$ deg, where vortex breakdown occurs. Careful examination of the $C_L - \alpha$ curve indicates the nonlinear behavior of the flowfield. Both the computations and the experiment show a decrease in lift curve slope at $\alpha \approx 15$ deg. The reason for this change is associated with the merging of the two vortices and is explained in Ref. 15. As seen in Fig. 5, there are two vortices over the wing, and they merge somewhere over the wing. Since two separate primary vortices make a larger contribution to the lift than one merged vortex, the lift is reduced once these vortices merge.

A critical change of lift occurs at $\alpha \approx 27$ deg with vortex breakdown. The exact angle of attack at which vortex breakdown occurs is sensitive to the initial condition, probably because of a hysteresis effect. The computed C_L values in Fig. 18 were obtained from a freestream initial condition. When started from the solution at $\alpha = 30$ deg, the computed value at $\alpha = 28$ deg becomes 0.912 ± 0.005, which is less than the value in Fig. 18. Similarly, the C_L value at $\alpha = 27$ deg becomes almost constant at 1.21 when started from the solution at $\alpha = 25$ deg and becomes 0.966 ± 0.004 when started from the solution at $\alpha = 28$ deg. The residual does not drop enough to obtain steady-state solutions for these cases, as described below, although the C_L values stay in a certain range even after 4000-8000 additional iterations. The causes of the observed hysteresis in the computed solutions may be related to the numerics. The effect of the outflow boundary condition and the location of the outer boundary cannot be discounted and should be investigated. However, it is highly probable that the hysteresis is physical. Numerous examples of hysteresis have been observed in experiments.[23-25] Future investigations may resolve this question.

The convergence history for $\alpha = 12$ deg is shown in Fig. 19 in terms of the C_L and the maximum residual. The time step was set to be constant ($\Delta t = 0.01$) and the computation was continued up to 5000 iterations in each case. At this angle of attack, the maximum residual drops more than three orders of

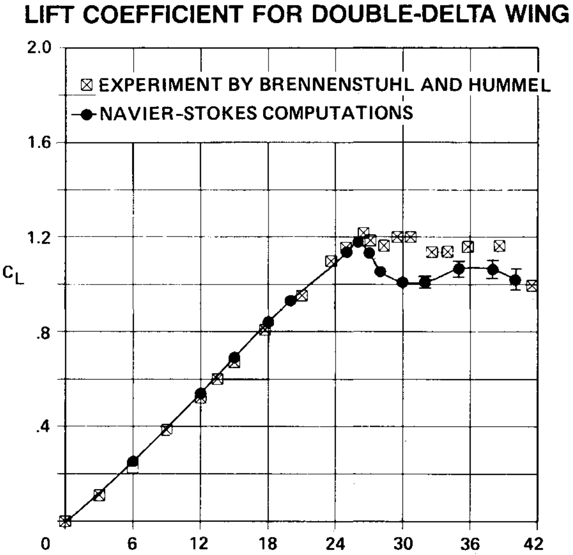

Fig. 18 C_L vs angle of attack: $M_\infty = 0.3$, $Re = 1.3 \times 10^6$.

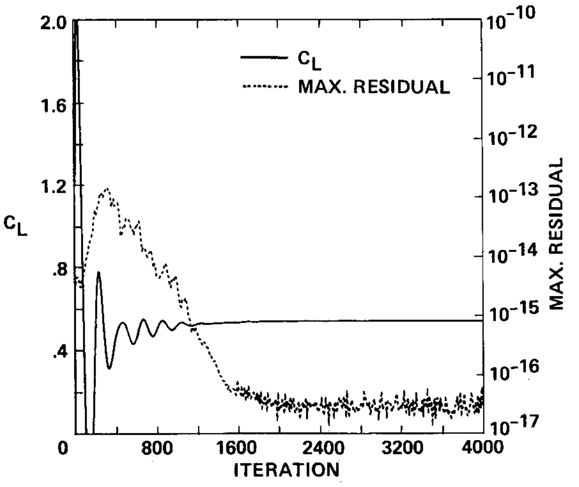

Fig. 19 C_L and maximum residual history for $\alpha = 12.0$ deg: $M_\infty = 0.3$, $Re = 1.3 \times 10^6$.

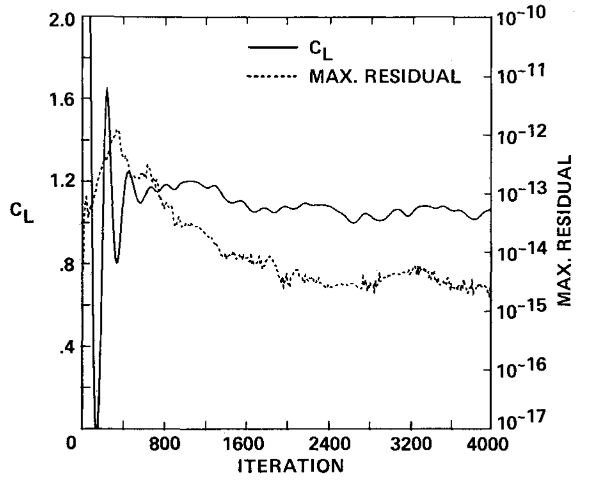

Fig. 20 C_L **and maximum residual history for** $\alpha = 35.0$ **deg:** $M_\infty = 0.3$, $Re = 1.3 \times 10^6$.

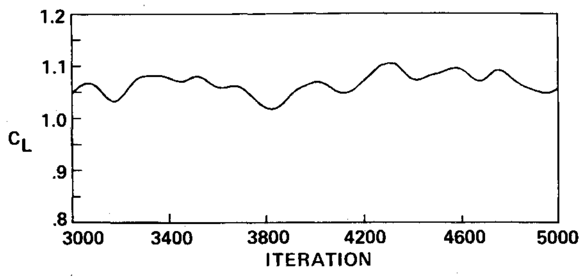

Fig. 21 **Close-up view of** C_L **oscillations during 4000–5000 iterations:** $\alpha = 35.0$ **deg:** $M_\infty = 0.3$, $Re = 1.3 \times 10^6$.

magnitude within 2000 iterations, and C_L becomes almost constant. The C_L is not strictly constant because there is small unsteadiness in the flowfield; however, the global flowfield is settled and does not change. A similar tendency is obtained for every angle of attack up to that at which vortex breakdown occurs. The C_L shows clear unsteadiness at angles of attack above the vortex breakdown incidence. Figure 20 shows the C_L and the maximum residual history for $\alpha = 35$ deg. The residual does not drop as much as that at $\alpha = 12$ deg, and the C_L become oscillatory. The C_L initially has strong oscillations and becomes settled after several hundred iterations. At about 1400 iterations, the C_L drops about 0.1, where the vortex breakdown seems to appear in the flowfield. From the C_L history, the breakdown seems to occur not abruptly but gradually in the flowfield. Figure 21 is a close-up of the C_L history, between 3000 and 5000 iterations. The C_L is oscillatory but stays in a certain range that is shown in Fig. 18. It is interesting that the range becomes larger as the angle of attack is increased. It should be noted that all of the figures above 30-deg angle of attack are instantaneous results at about 5000 iterations.

There may be a concern about using the diagonal form LU-ADI solution method in unsteady computations since the algorithm is at best first-order accurate and nonconservative in time. However, in the present study, quantitative study of the time-dependent response is not the primary interest. The main interest is associated with qualitative comparison. In addition, the flow oscillations observed are slow and shock free. As a result, the use of the diagonal form should be adequate.

Euler Solutions

The inviscid Euler equations have been widely used for vortical flow simulations even though such methods cannot properly take into account the vorticity generated in the attached boundary layers. To assess the capability of the Euler methods for the present vortical flows, several Euler computations were carried out under the same conditions. The code was the same as that used for the Navier-Stokes computations except that the viscous terms were deleted and the surface tangency condition was imposed instead of the no-slip condition. The grid used was identical to the fine grid used for the Navier-Stokes computations. In addition, the smoothing terms were set to be similar. Figure 18 shows that, in general, the lift coefficient from the Euler results are lower than those of both the Navier-Stokes solutions and of the experiment. At $\alpha = 12$ deg, the Euler solution showed very weak vortical flow and the two vortices did not merge even at the trailing edge. The inviscid Euler result at $\alpha = 30$ deg showed clear vortical flow but failed to predict vortex breakdown, in contrast to the Navier-Stokes solution. At $\alpha = 35$ deg, the Euler results showed vortex breakdown. Details of the Euler results are given in Ref. 21.

Additional Remarks

To understand the flow inside the vortex breakdown, two dynamic graphics packages, RIP and GAS, developed at the Ames Research Center, were intensively used. The interactive RIP package showed us how the flow is directed inside the reverse-flow region. The size and the location of the breakdown were better understood with animation using GAS. The use of both the graphics workstations and the dynamic graphics software is very important and helps to enhance our understanding of computed flowfield.

Two supercomputers, the Cray 2 at Ames and the Amdahl 1200 at the Amdahl Corporation, were used for this study. Fine-grid Navier-Stokes solutions showing vortex breakdown were obtained on the Cray 2 supercomputer, which has a maximum speed of 1700 MFLOPS for four processors. One computation at $\alpha = 12$ deg was carried out on both machines, and the computed C_P distributions were within plotting accuracy. The remainder of the computations was carried out on the Amdahl 1200, which has a maximum speed of 570 MFLOPS. The code required 8.6 μs per grid point per iteration on Amdahl 1200 and 20.0 μs on a single processor of the Cray 2.

Concluding Remarks

Computations of vortical flows over a strake-delta wing have been carried out using the three-dimensional, thin-layer Navier-Stokes equations at low Mach number. A fine-mesh distribution with 850,000 grid points was used to capture the physical phenomenon. Computations were carried out for angles of attack ranging from 6–40 deg. Over this range of angle of attack, the computed lift coefficients were in good agreement with the experimental data. A computed result at $\alpha = 12$ deg showed the interaction process of the vortex emanating from the strake leading edge with that from the wing leading edge. The computation at $\alpha = 30$ deg indicated that bubble-type vortex breakdown occurs near the trailing edge of the wing, whereas at $\alpha = 35$ deg, the spiral type of vortex breakdown was obtained. An intensive study using sophisticated graphics programs revealed some features of the breakdown phenomenon. Comparison of the computed results with the experiment shows that qualitative features of the flow are well simulated when a fine mesh is used. The result also indicates the importance of grid resolution in simulating vortical flows. Still better resolution is necessary to obtain better quantitative results for this complicated flowfield.

Acknowledgment

Because of the large number of grid points, this study required extensive CPU time. The authors would like to express their gratitude to the Amdahl Corporation for allowing them to use the VPS system. The authors would also like to thank Dr. J. L. Steger and Dr. W. R. Van Dalsem of Ames Research Center for stimulating discussions during this study.

References

[1]Fujii, K. and Kutler, P., "Numerical Simulation of the Viscous Flow over Three-Dimensional Complicated Geometries," AIAA Paper 84-1550, June 1984.

[2]Rizzetta, D. P. and Shang, J. S., "Numerical Simulation of Leading Edge Vortical Flows," AIAA Paper 84-1544, June 1984.

[3]Hartwich, P. M. and Hsu, C. H., "An Implicit Flux-Difference Splitting Scheme for Three-Dimensional Incompressible Navier-Stokes Solutions to Leading Edge Vortex Flows," AIAA Paper 86-1839-CP, June 1986.

[4]Thomas, J. L., Taylor, S. L., and Anderson W. K., "Navier-Stokes Computations of Vortical Flows Over Low Aspect Ratio Wings," AIAA Paper 87-0207, June 1987.

[5]Newsome, R. W., "A Comparison of Euler and Navier-Stokes Solutions for Supersonic Flow Over a Conical Delta Wing," AIAA Paper 85-0111, Jan. 1985.

[6]Fujii, K. and Obayashi, S., "Evaluation of Euler and Navier-Stokes Solutions for Leading-Edge and Shock-Induced Separations," AIAA Paper 85-1563, July 1985.

[7]Chakravarthy, S. R. and Ota, D. K., "Numerical Issues in Computing Inviscid Supersonic Flow Over Conical Delta Wings," AIAA Paper 86-0440, Jan. 1986.

[8]Powell, K., Murman, E. M., Perez, E., and Baron J., "Total Pressure Loss in Vortical Solutions of the Conical Euler Equations," AIAA Paper 85-1701, July 1985.

[9]Raj, P., Sikora, J. S., and Keen, J. M., "Free-Vortex Simulation Using a Three-Dimensional Euler Aerodynamic Method," *Journal of Aircraft*, Vol. 25, No. 2, Feb. 1988, pp. 128–134.

[10]Fujii, K. and Obayashi, S., "Navier-Stokes Simulations of Transonic Flows Over a Practical Wing Configuration," *AIAA Journal*, Vol. 25, March 1987, pp. 369–370.

[11]Fujii, K. and Obayashi, S., "Navier-Stokes Simulations of Transonic Flows Over a Wing-Fuselage Combination," *AIAA Journal*, Vol. 25, Dec. 1987, pp. 1587–1596.

[12]Pulliam, T. H. and Steger, J. L., "Implicit Finite Difference Simulations of Three-Dimensional Compressible Flows," *AIAA Journal*, Vol. 18, Feb. 1980, pp. 159–167.

[13]Pulliam, T. H. and Steger, J. L., "Recent Improvement in Efficiency, Accuracy, and Convergence for Implicit Approximate Factorization Algorithms," AIAA Paper 85-360, Jan. 1985.

[14]Steger, J. L. and Warming, R. F., "Flux Vector Splitting of the Inviscid Gas-Dynamic Equations with Application to Finite-Difference Methods," *Journal of Computational Physics*, Vol. 40, No. 2, April 1981, pp. 263–293.

[15]Brennenstuhl, U. and Hummel, D., "Vortex Formation Over Double-Delta Wings," *Proceedings of the 13th Congress of the International Council of the Aeronautical Sciences*, ICAS Paper 82-6.6.3, Aug. 1982.

[16]Thompson, D. H., "A Visualization Study of the Vortex Flow around Double-Delta Wings," Aeronautical Research Laboratories, Melbourne, Australia, ARL-AERO-R-165, Aug. 1985.

[17]Steger, J. L. and Rizk, Y. M., "Generation of Three-Dimensional Body-Fitted Coordinates Using Hyperbolic Partial Differential Equations," NASA TM-86753, June 1985.

[18]Hummel, D., "On the Vortex Formation over a Slender Wing at Large Angles of Incidence," *High Angle of Attack Aerodynamics*, AGARD CP-247, Paper 15, Oct. 1978.

[19]Degani, D. and Schiff, L. B., "Computation of Turbulent Supersonic Flows Around Pointed Bodies Having Crossflow Separation," *Journal of Computational Physics*, Vol. 66, No. 1, Sept. 1986, pp. 173–196.

[20]Rai, M. M., "Navier-Stokes Simulations of Blade-Vortex Interaction Using High-Order Accurate Upwind Schemes," AIAA Paper 87-0543, 1987.

[21]Fujii, K., Gavali, S., and Holst, T. L., "Evaluation of Navier-Stokes and Euler Solutions for Leading-Edge Separation Vortices," *Proceedings of the 5th International Conference on Numerical Methods in Laminar and Turbulent Flow*, July 1987.

[22]Payne, F. M., Ng, T. T., Nelson, R. C., and Schiff, L. B., "Visualization and Wake Surveys of Vortical Flow over a Delta Wing," *AIAA Journal*, Vol. 26, Feb. 1988, pp. 137–143.

[23]Lowson, M. V., "Some Experiments with Vortex Breakdown," *Journal of the Royal Aeronautical Society*, Vol. 68, No. 641, May 1964, pp. 343–346.

[24]Elle, B. J., "An Investigation at Low Speed of the Flow Near the Apex of Thin Delta Wings with Sharp Leading Edges," Aeronautical Research Council, Reports and Memoranda No. 3176, A.R.C. 19780, 1961.

[25]Wendt, J. F., "Compressibility Effects on Flow Around Simple Components," *High Angle of Attack Aerodynamnics*, AGARD LS-121, Paper 7, March 1982.